JOURNAL OF AIRCRAFT
Vol. 44, No. 5, September–October 2007

# Optimum Shape Design for Unsteady Three-Dimensional Viscous Flows Using a Nonlinear Frequency-Domain Method

Siva K. Nadarajah*
*McGill University, Montreal, Quebec H3A 2S6, Canada*
and
Antony Jameson†
*Stanford University, Stanford, California 94305*

DOI: 10.2514/1.27601

**This paper presents an adjoint method for the optimum shape design of unsteady three-dimensional viscous flows. The goal is to develop a set of discrete unsteady adjoint equations and the corresponding boundary condition for the nonlinear frequency-domain method. First, this paper presents the complete formulation of the time-dependent optimal design problem. Second, we present the nonlinear frequency-domain adjoint equations for three-dimensional viscous transonic flows. Third, we present results that demonstrate the application of the theory to a three-dimensional wing.**

## Nomenclature

| | | |
|---|---|---|
| $b$ | = | boundary velocity component |
| $d$ | = | artificial dissipation flux |
| $E$ | = | internal energy |
| $F$ | = | numerical flux vector |
| $f$ | = | flux vector |
| $\mathcal{G}$ | = | gradient |
| $I$ | = | cost function |
| $i, j$ | = | cell indices |
| $k$ | = | wave number |
| $M$ | = | Mach number |
| $p$ | = | pressure |
| $R$ | = | residual |
| $\hat{R}$ | = | Fourier coefficient of residual |
| $\mathcal{S}$ | = | shape function |
| $S$ | = | face areas of the computational cell |
| $t$ | = | time |
| $t_f$ | = | final time |
| $u$ | = | velocity (physical domain) |
| $V$ | = | cell volume |
| $w$ | = | state vector |
| $\hat{w}$ | = | Fourier coefficient of the state vector |
| $x$ | = | coordinates (physical domain) |
| $\alpha$ | = | angle of attack |
| $\xi$ | = | coordinates (computational domain) |
| $\rho$ | = | density |
| $\sigma$ | = | viscous stress |
| $\psi$ | = | Lagrange multiplier |
| $\omega_r$ | = | reduced frequency |

## I. Introduction

THE majority of work in aerodynamic shape optimization has been focused on the design of aerospace vehicles in a steady-flow environment. Investigators have applied these advanced design algorithms, particularly the adjoint method, to numerous problems, ranging from the design of two-dimensional airfoils to full aircraft configurations to decrease drag, increase range, and reduce sonic boom [1–5]. These problems were tackled using many different numerical schemes on both structured and unstructured grids.

Unlike fixed-wing aircraft, helicopter rotors and turbomachinery blades operate in unsteady flow and are constantly subjected to unsteady loads. Therefore, optimal control techniques for unsteady flows are needed to improve the performance of helicopter rotors and turbomachinery and to alleviate the unsteady effects that contribute to flutter, buffeting, poor gust and acoustic response, and dynamic stall. As yet, there have been few efforts in this direction.

The demanding computational cost associated with the calculation of unsteady three-dimensional flows is one of the major reasons for the absence of optimization techniques to improve performance. It was estimated[‡] that the computational cost of a typical multistage compressor and turbine calculation using parallel processing of 750 processors working 8 h a day would take over 1300 days (estimates are based on the flow through a 23-blade row compressor). Even though most of the computational time in periodic problems is spent in resolving the decay of the initial transients, engineers are typically only concerned with the data once the solution has reached a periodic steady state. As a result, there has been much effort focused on the development of efficient and practical alternatives to the study of unsteady periodic problems. Although this example is an extreme case, it illustrates the prohibitive cost of many unsteady calculations using time-accurate solvers to find a periodic steady state.

Nevertheless, Nadarajah and Jameson [6,7] pursued the development of optimum shape design for two- and three-dimensional unsteady flows using the time-accurate adjoint-based design approach. This work is largely based on algorithms developed for aerodynamic shape optimization for the steady-flow environment. Nadarajah derived and applied the time-accurate adjoint equations (both the continuous and discrete) to the redesign of an oscillating airfoil in an inviscid transonic flow. The redesigned shape achieved a reduction in the time-averaged drag while maintaining the time-averaged lift. The approach used a dual time-stepping [8] technique that implements a fully implicit, second-order, backward-

Presented as Paper 3455 at the 25th Applied Aerodynamics Conference, San Francisco, 5–8 June 2006; received 31 August 2006; revision received 29 November 2006; accepted for publication 18 October 2006. Copyright © 2007 by the American Institute of Aeronautics and Astronautics, Inc. All rights reserved. Copies of this paper may be made for personal or internal use, on condition that the copier pay the $10.00 per-copy fee to the Copyright Clearance Center, Inc., 222 Rosewood Drive, Danvers, MA 01923; include the code 0021-8669/07 $10.00 in correspondence with the CCC.

*Assistant Professor, Computational Fluid Dynamics Lab, Department of Mechanical Engineering, 688 Sherbrooke Street West, Room 711; siva.nadarajah@mcgill.ca.

†Thomas V. Jones Professor of Engineering, Department of Aeronautics and Astronautics, Durand Building, 496 Lomita Mall. Fellow AIAA.

‡Personal communications on TFLO with R. Davis, January–December 2001.

difference formula to discretize the time derivative. Typical runs required 15 periods with 24 discrete time steps per period and 15 multigrid cycles at each time step. Encouraging results were obtained at a substantial computational expense.

The prohibitive cost of computing three-dimensional unsteady flows using the time-accurate approach has motivated a new interest in using periodic methods. Linearized frequency-domain and deterministic stress methods [9] are examples of periodic methods that are widely used in industry. Unfortunately, the inability of these methods to accurately model the solution becomes evident for systems that contain strong nonlinearities. The harmonic balance technique, a pseudospectral approach initially proposed by Hall et al. [10] and later modified by McMullen et al. [11,12], was validated against both the Euler and Navier–Stokes equations for a number of unsteady periodic problems. The cost associated with spectral methods like the McMullen et al. nonlinear frequency-domain method (NLFD) is proportional to the cost of the steady-state solution multiplied by the number of desired temporal modes. The ability of the NLFD method to account for strong nonlinearities and converge to the exact solution exponentially is the reason why it is used in this work to solve for the transonic flutter boundary of a NACA64A010 airfoil. For inviscid flow, it was shown by McMullen [13] that to accurately model an oscillating airfoil pitching about its quarter-chord, a temporal resolution of only one mode above the fundamental frequency (or, equivalently, three time samples per period) is needed using the NLFD method versus the 45 time samples needed with a backward-difference formulation of the time derivative [8].

These results demonstrate the potential of the method to provide significant reduction in computational cost for the analysis and design of more realistic problems such as helicopter rotors, turbomachinery, and other unsteady devices operating in the transonic regime. Nadarajah et al. [14] extended their two-dimensional optimum shape design for unsteady flows from a time-accurate scheme to the NLFD approach, in the process, developing the NLFD adjoint equations. The method was further extended for three-dimensional inviscid flows and presented in [15]. The modeling of unsteady aerodynamic design sensitivities using either the harmonic balance technique or the nonlinear frequency-domain approach was also investigated by Duta et al. [16] and Thomas et al. [17]. Duta et al. [16] presented a harmonic adjoint approach for unsteady turbomachinery design. The aim of the work was to reduce blade vibrations due to flow unsteadiness. The research produced adjoint methods that were based on a linearized analysis of periodic unsteady flows. Thomas et al. [17] presented a viscous discrete adjoint approach for computing unsteady aerodynamic design sensitivities. The adjoint code was generated from the harmonic balance flow solver with the use of an automatic differentiation software compiler.

The work presented in this paper is a viscous extension of an inviscid [15] capability. We will explore the required number of time steps per period to accurately resolve the unsteady flowfield and examine the effect of temporal resolution on the accuracy of the gradient. The motivation of the research was fueled both by the success of our current capability for automatic shape optimization for unsteady flows and the future potential of the NLFD method. The result of this effort is a NLFD adjoint design code that is fully nonlinear and a computational cost of the adjoint module that is proportional to the cost of the flow solver.

## II. Governing Equations

The Cartesian coordinates and velocity components are denoted by $x_1$, $x_2$, and $x_3$ and $u_1$, $u_2$, and $u_3$. Einstein notation simplifies the presentation of the equations, in which summation over $i = 1$ to 3 is implied by a repeated index $i$. The three-dimensional Navier–Stokes equations then take the form

$$\frac{\partial w}{\partial t} + \frac{\partial f_i}{\partial x_i} = \frac{\partial f_{vi}}{\partial x_i} \qquad \text{in } \mathcal{D} \tag{1}$$

where the state vector $w$, inviscid flux vector $f$, and viscous flux vector $f_v$ are, respectively, described by

$$w = \begin{Bmatrix} \rho \\ \rho u_1 \\ \rho u_2 \\ \rho u_3 \\ \rho E \end{Bmatrix}$$

$$f_i = \begin{Bmatrix} \rho(u_i - b_i) \\ \rho u_1(u_i - b_i) + p\delta_{i1} \\ \rho u_2(u_i - b_i) + p\delta_{i2} \\ \rho u_3(u_i - b_i) + p\delta_{i3} \\ \rho E(u_i - b_i) + p u_i \end{Bmatrix}, \quad \text{and} \quad f_{vi} = \begin{Bmatrix} 0 \\ \sigma_{ij}\delta_{j1} \\ \sigma_{ij}\delta_{j2} \\ \sigma_{ij}\delta_{j3} \\ u_j\sigma_{ij} + k\frac{\partial T}{\partial x_i} \end{Bmatrix} \tag{2}$$

In these definitions, $b_i$ are the Cartesian velocity components of the boundary, and $\delta_{ij}$ is the Kronecker delta function. The pressure is determined by the equation of state

$$p = (\gamma - 1)\rho\left\{E - \frac{1}{2}(u_i u_i)\right\}$$

and the stagnation enthalpy is given by

$$H = E + \frac{p}{\rho}$$

where $\gamma$ is the ratio of the specific heats. The viscous stresses may be written as

$$\sigma_{ij} = \mu\left(\frac{\partial u_i}{\partial x_j} + \frac{\partial u_j}{\partial x_i}\right) + \lambda\delta_{ij}\frac{\partial u_k}{\partial x_k} \tag{3}$$

where $\mu$ is the sum of the laminar coefficient of viscosity and the eddy viscosity and $\lambda$ is the second coefficient of viscosity. A Baldwin–Lomax turbulence model is employed to compute the eddy viscosity. The coefficient of thermal conductivity and the temperature are computed as

$$k = \frac{c_p\mu}{Pr}, \qquad T = \frac{p}{\mathcal{R}\rho} \tag{4}$$

where $Pr$ is the Prandtl number, $c_p$ is the specific heat at constant pressure, and $\mathcal{R}$ is the gas constant.

For discussion of real applications using a discretization on a body-conforming structured mesh, it is also useful to consider a transformation to the computational coordinates $\xi_1$, $\xi_2$, and $\xi_3$, defined by the metrics

$$K_{ij} = \left[\frac{\partial x_i}{\partial \xi_j}\right], \qquad J = \det(K), \qquad K_{ij}^{-1} = \left[\frac{\partial \xi_i}{\partial x_j}\right]$$

The simulations contained in this research are restricted to rigid-mesh translation. As a result, we can write Eq. (1) as the product of the cell volume and temporal derivative of the state vector $w$ at the cell center. In terms of cell volumes and the local residual $R(w)$ (comprising both convective and dissipative fluxes), Eq. (1) can be written in semidiscrete form as

$$V\frac{\partial w}{\partial t} + R(w) = 0 \qquad \text{in } \mathcal{D} \tag{5}$$

where the residual $R(w)$ can then be written in computational space as

$$R(w) = \frac{\partial(F_i - F_{vi})}{\partial \xi_i} \tag{6}$$

where the inviscid and viscous flux contributions are now defined with respect to the computational cell faces by $F_i = S_{ij}f_j$ and $F_{vi} = S_{ij}f_{vj}$, and the quantity $S_{ij} = JK_{ij}^{-1}$ represents the projection

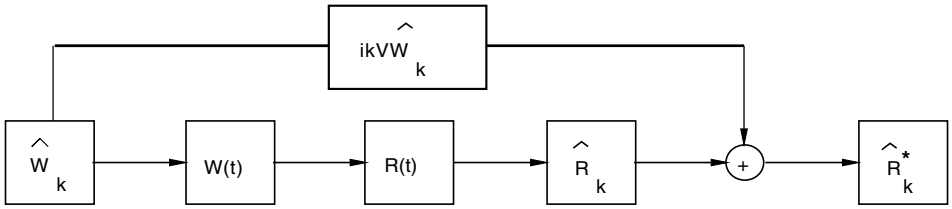


**Fig. 1 Simplified data flow diagram of the time-advancement scheme illustrating the pseudospectral approach used in calculating the nonlinear spatial operator *R*.**

of the $\xi_i$ cell face along the $x_j$ axis. In obtaining Eq. (6) we have made use of the property that

$$\frac{\partial S_{ij}}{\partial \xi_i} = 0 \tag{7}$$

which represents the fact that the sum of the face areas over a closed volume is zero, as can be readily verified by a direct examination of the metric terms.

When Eq. (6) is formulated for each computational cell, a system of first-order ordinary differential equations is obtained. To eliminate odd–even decoupling of the solution and overshoots before and after shock waves, the conservative and viscous fluxes are added to a diffusion flux. The artificial dissipation scheme used in this research is a blended first- and third-order flux, first introduced by Jameson et al. [18]. The blended first- and third-order artificial dissipation term is discretized as

$$d_{i+\frac{1}{2},j,k} = \nu^{(2)}_{i+\frac{1}{2},j,k}\Lambda_{i+\frac{1}{2},j,k}\Delta_{i+\frac{1}{2},j,k} - \nu^{(4)}_{i+\frac{1}{2},j,k}\Lambda_{i+\frac{1}{2},j,k}[\Delta_{i+\frac{3}{2},j,k} - 2\Delta_{i+\frac{1}{2},j,k} + \Delta_{i-\frac{1}{2},j,k}].$$

where

$$\Delta_{i+\frac{1}{2},j,k} = w_{i+1,j,k} - w_{i,j,k}$$

the coefficients $\nu^{(2)}$ and $\nu^{(4)}$ are the products of the adjustable constants and the normalized second difference of the pressure, and $\Lambda_{i+\frac{1}{2},j,k}$ is the rescaled numerical spectral radius of the flux Jacobian matrix and directionally scales the dissipative terms.

## III. General Formulation of the Time-Dependent Optimal Design Problem

The aerodynamic properties that define the cost function are functions of the flowfield variables, $w$, and the physical location of the boundary, which may be represented by the function $\mathcal{S}$. We then introduce the cost function

$$I = \frac{1}{T}\int_0^{t_f} \mathcal{L}(w, \mathcal{S})\,\mathrm{d}t + \mathcal{M}[w(t_f)] \tag{8}$$

The cost function is a sum of a time-averaged function, $\mathcal{L}(w, \mathcal{S})$, and a function $\mathcal{M}$ that is a function of the solution $w(t)$ at the final time. Then a change in $\mathcal{S}$ results in a change

$$\delta I = \frac{1}{T}\int_0^{t_f}\left(\frac{\partial \mathcal{L}^T}{\partial w}\delta w + \frac{\partial \mathcal{L}^T}{\partial \mathcal{S}}\delta \mathcal{S}\right)\mathrm{d}t + \frac{\partial \mathcal{M}^T}{\partial w}\delta w(t_f) \tag{9}$$

in the cost function. Using control theory, the governing equations of the flowfield are now introduced as a constraint in such a way that the final expression for the gradient does not require reevaluation of the flowfield. To achieve this, $\delta w$ must be eliminated from Eq. (9). From Eq. (5), a variation of the semidiscrete form of the governing equations can be written as

$$V\frac{\partial}{\partial t}\delta w + \left[\frac{\partial R}{\partial w}\right]\delta w + \left[\frac{\partial R}{\partial \mathcal{S}}\right]\delta \mathcal{S} = 0$$

Next, introduce a Lagrange multiplier $\psi$ to the time-dependent flow equation and integrate it over time, to yield

$$\frac{1}{T}\int_0^{t_f}\psi^T\left(V\frac{\partial}{\partial t}\delta w + \left[\frac{\partial R}{\partial w}\right]\delta w + \left[\frac{\partial R}{\partial \mathcal{S}}\right]\delta \mathcal{S}\right) = 0 \tag{10}$$

Subtract Eq. (10) from the variation of the cost function to arrive at the following equation:

$$\delta I = \frac{1}{T}\int_0^{t_f}\left(\frac{\partial \mathcal{L}^T}{\partial w}\delta w + \frac{\partial \mathcal{L}^T}{\partial \mathcal{S}}\delta \mathcal{S}\right)\mathrm{d}t + \frac{\partial \mathcal{M}^T}{\partial w}\delta w(t_f) - \frac{1}{T}\int_0^{t_f}\psi^T\left(V\frac{\partial}{\partial t}\delta w + \left[\frac{\partial R}{\partial w}\right]\delta w + \left[\frac{\partial R}{\partial \mathcal{S}}\right]\delta \mathcal{S}\right)\mathrm{d}t \tag{11}$$

Next, collect the $\delta w$ and $\delta \mathcal{S}$ terms and integrate

$$\frac{1}{T}\int_0^{t_f}\psi^T V\frac{\partial}{\partial t}\delta w\,\mathrm{d}t$$

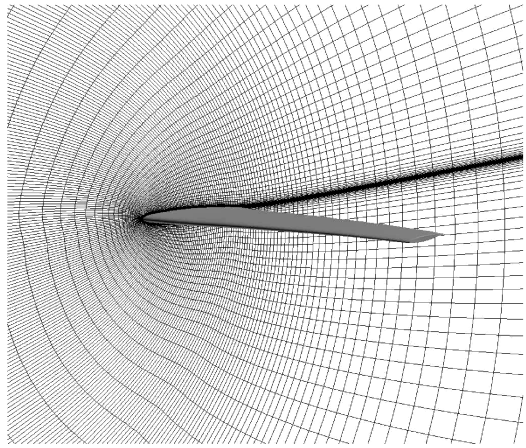

**a) LANN Wing mesh**

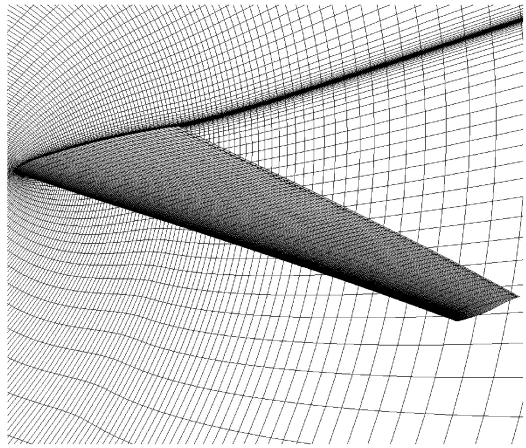

**b) Close-Up view**

**Fig. 2 LANN wing grid structure; MPI domain topology, $N_{p_i} = 4$, $N_{p_j} = 1$, and $N_{p_k} = 3$; grid size $n_x \times n_j \times n_k = 257 \times 65 \times 97$.**

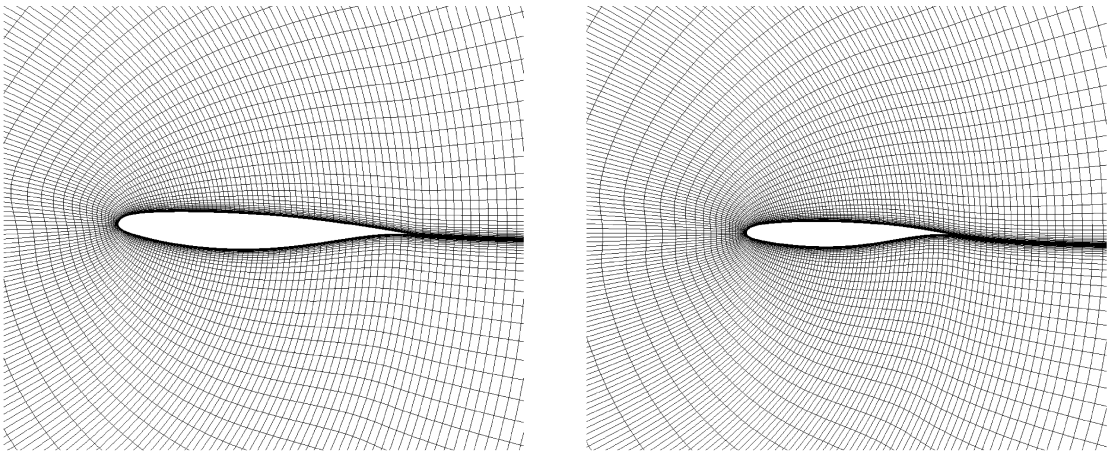

a) Mesh Cross Section at 20% Span b) Mesh Cross Section at 65% Span

**Fig. 3 LANN wing mesh; grid size $n_x \times n_j \times n_k = 257 \times 65 \times 97$.**

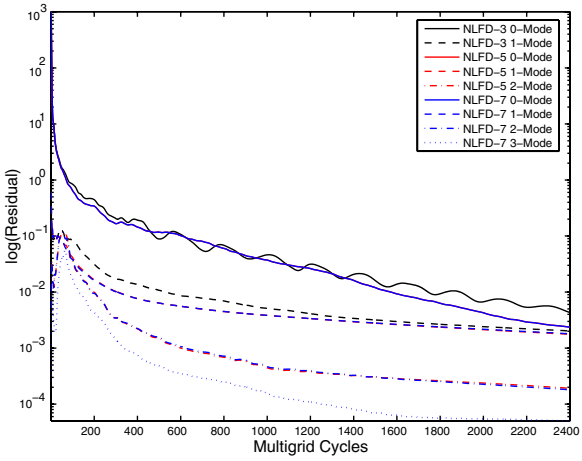


**Fig. 4 Viscous NLFD flow solver convergence.**

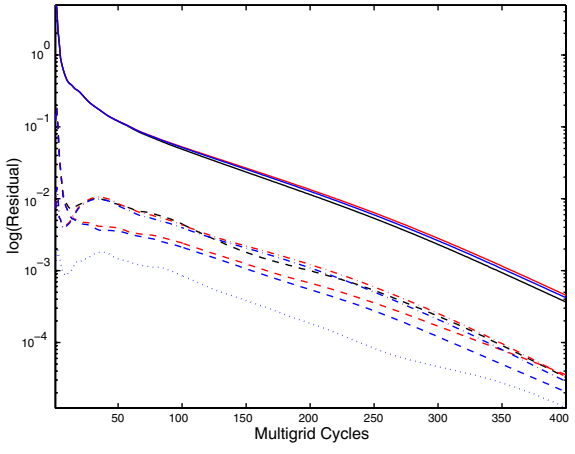


**Fig. 5 Viscous NLFD adjoint solver convergence.**

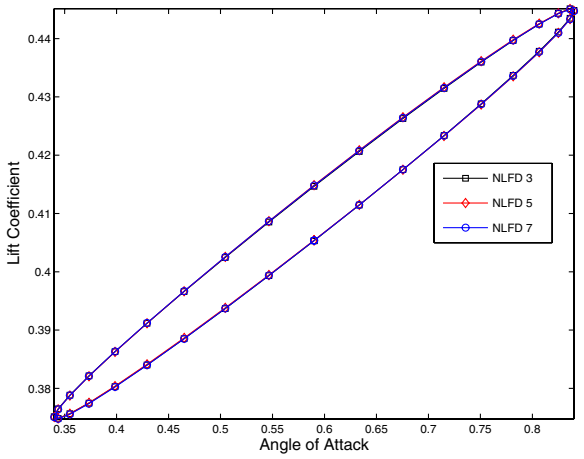


**Fig. 6 Comparison of lift hysteresis for various modes; LANN wing, run 73.**

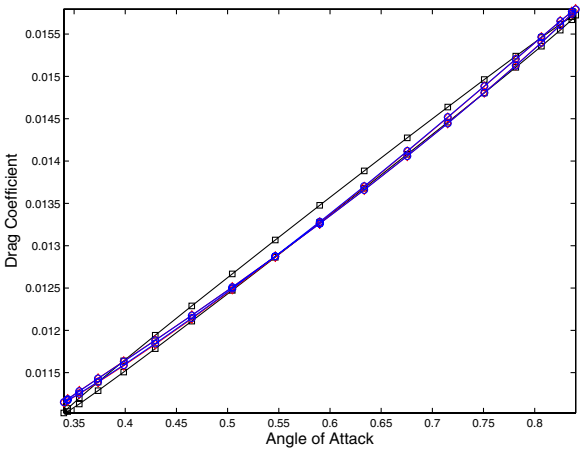


**Fig. 7 Comparison of variation of drag coefficient vs angle of attack for various modes; LANN wing, run 73.**

by parts, to yield

$$\delta I = \frac{1}{T}\int_0^{t_f}\left(\frac{\partial \mathcal{L}^T}{\partial w} + V\frac{\partial \psi^T}{\partial t} - \psi^T\left[\frac{\partial R}{\partial w}\right]\right)\delta w\,\mathrm{d}t + \left[\frac{\partial \mathcal{M}^T}{\partial w} - \frac{V}{T}\psi^T(t_f)\right]\delta w(t_f) + \frac{1}{T}\int_0^{t_f}\left(\frac{\partial \mathcal{L}^T}{\partial \mathcal{S}} - \psi^T\left[\frac{\partial R}{\partial \mathcal{S}}\right]\right)\delta \mathcal{S}\,\mathrm{d}t$$

Choose $\psi$ to satisfy the adjoint equation

$$V\frac{\partial \psi}{\partial t} - \left[\frac{\partial R}{\partial w}\right]^T\psi = -\frac{\partial \mathcal{L}}{\partial w}$$

with the terminal boundary condition $\frac{V}{T}\psi(t_f) = \partial\mathcal{M}/\partial w$. Then the variation of the cost function reduces to

$$\delta I = \mathcal{G}^T\delta \mathcal{S}$$

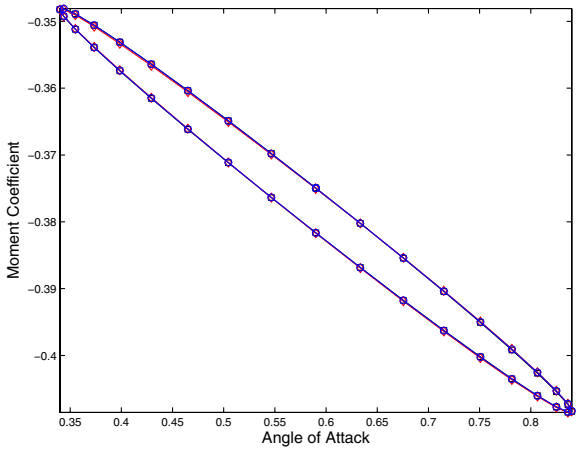


**Fig. 8 Comparison of variation of pitching moment coefficient vs angle of attack for various modes; LANN wing, run 73.**

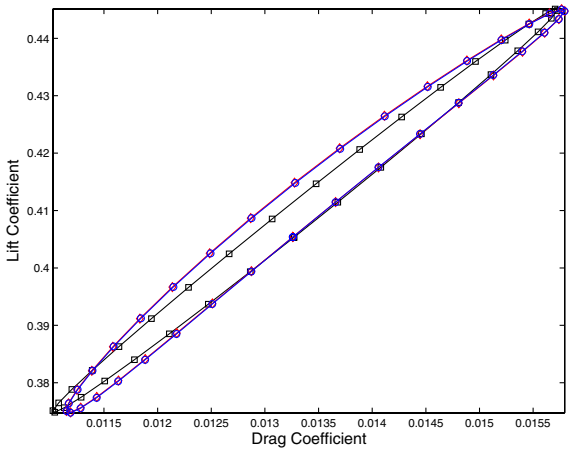


**Fig. 9 Comparison of lift vs drag coefficient for various modes; LANN wing, run 73.**

where

$$\mathcal{G}^{\mathcal{T}} = \frac{1}{T}\int_0^{t_f}\left(\frac{\partial \mathcal{L}^T}{\partial \mathcal{S}} - \psi^T \frac{\partial R}{\partial \mathcal{S}}\right) \mathrm{d}t$$

Optimal control of time-dependent trajectories is generally complicated by the need to solve the adjoint equation in reverse time from a final boundary condition using data from the trajectory solution, which in turn depends on the control derived from the adjoint solution. The sensitivities are determined by the solution of the adjoint equation in reverse time from the terminal boundary condition and the time-dependent solution of the flow equation. These sensitivities are then used to get a direction of improvement and steps are taken until convergence is achieved.

## IV. Development of the Nonlinear Frequency-Domain Adjoint Equations

The derivation of the NLFD method starts with the semidiscrete form of the governing equations and assumes that the solution $w$ and

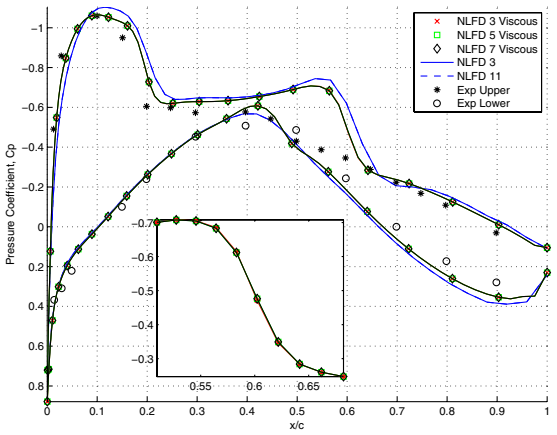


**a) $\eta$=20%, $\alpha$=$\alpha_{mean}$=0.59 deg**

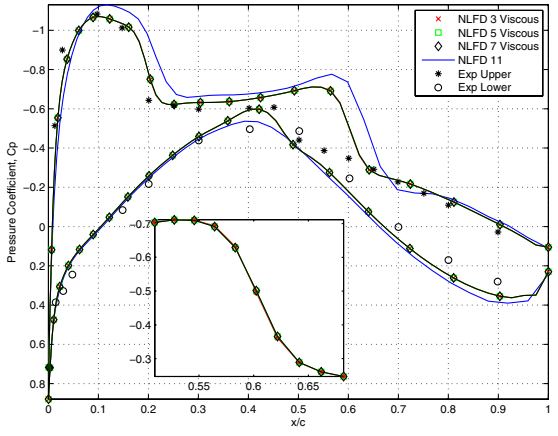


**b) $\eta$=20%, $\alpha$=$\alpha_{max}$=0.84 deg**

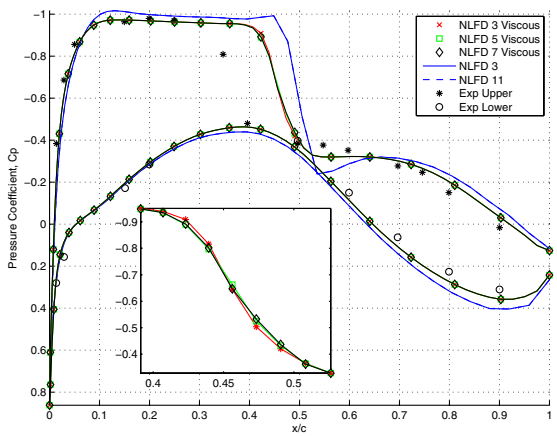


**c) $\eta$=65%, $\alpha$=$\alpha_{mean}$=0.59 deg**

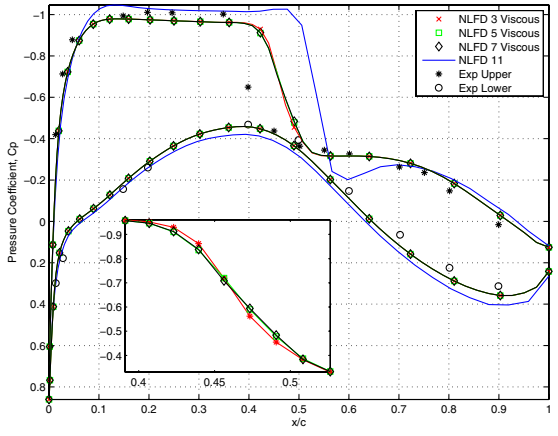


**d) $\eta$=65%, $\alpha$=$\alpha_{max}$=0.84 deg**

**Fig. 10 Comparison of pressure distribution between inviscid, viscous, and experimental data for the LANN wing, run 73.**

spatial operator $R$ can be represented by separate Fourier series:

$$w = \sum_{k=-\frac{N}{2}}^{\frac{N}{2}-1} \hat{w}_k e^{ikt}, \qquad R = \sum_{k=-\frac{N}{2}}^{\frac{N}{2}-1} \hat{R}_k e^{ikt} \tag{12}$$

where $i = \sqrt{-1}$.

Here, however, each coefficient $\hat{R}_k$ of the transform of the residual depends on all the coefficients $\hat{w}_k$, because $R[w(t)]$ is a nonlinear function of $w(t)$. Thus, Eq. (13) represents a nonlinear set of equations that must be iteratively solved. The solver attempts to find a solution $w$ that drives this system of equations to zero for all wave numbers, but at any iteration in the solution process, the unsteady residual $R^*$ will be finite:

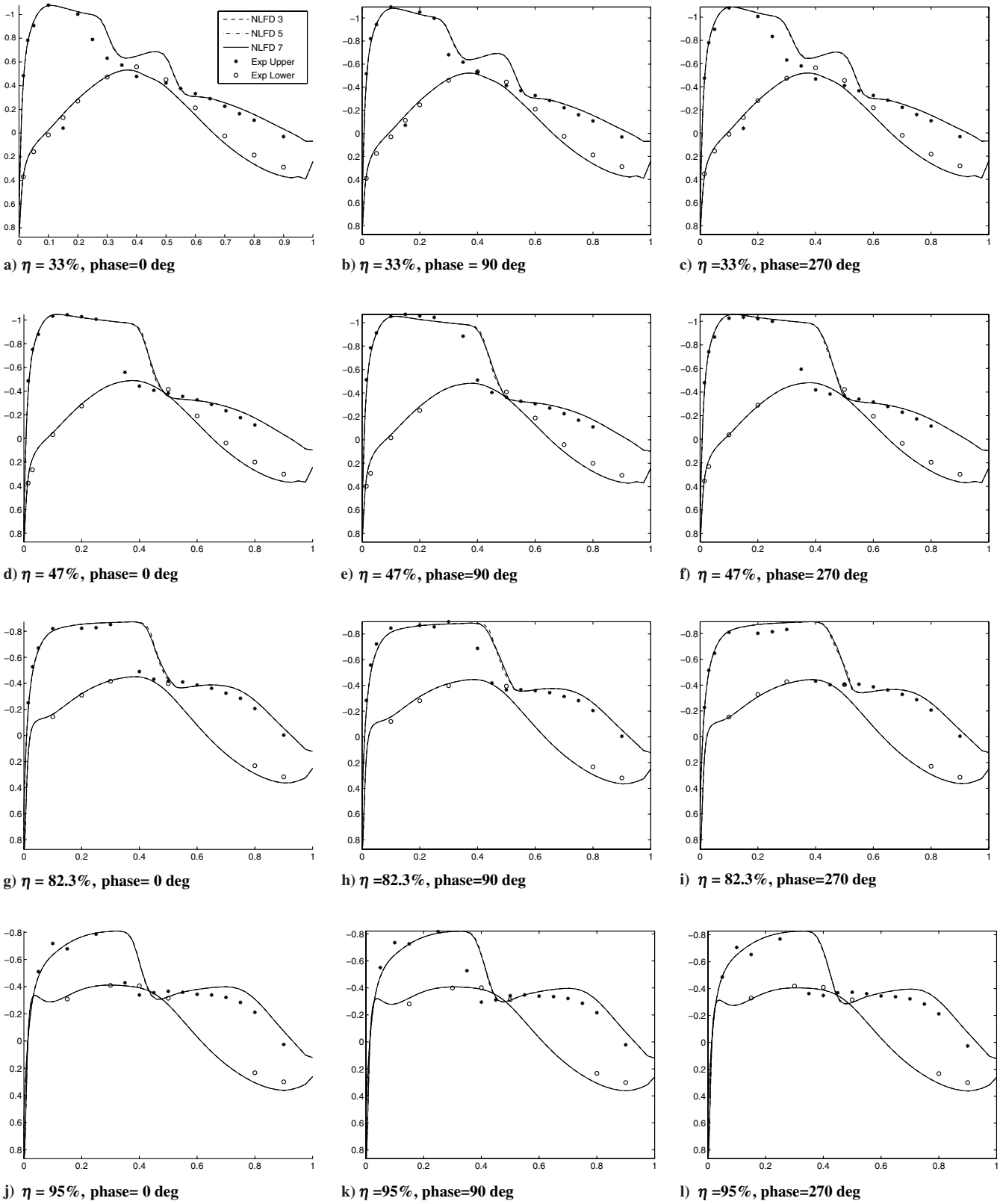


a) $\eta$ = 33%, phase=0 deg  b) $\eta$ = 33%, phase = 90 deg  c) $\eta$ =33%, phase=270 deg

d) $\eta$ = 47%, phase= 0 deg  e) $\eta$ = 47%, phase=90 deg  f) $\eta$ = 47%, phase= 270 deg

g) $\eta$ = 82.3%, phase= 0 deg  h) $\eta$ =82.3%, phase=90 deg  i) $\eta$ = 82.3%, phase=270 deg

j) $\eta$ = 95%, phase= 0 deg  k) $\eta$ =95%, phase=90 deg  l) $\eta$ =95%, phase=270 deg

**Fig. 11 Comparison of pressure distribution for various time steps for the LANN wing, run 73**

$$\hat{R^*}_k = ikV\hat{w}_k + \hat{R}_k \tag{13}$$

The nonlinearity of the unsteady residual stems from the spatial operator. There are two approaches to calculating the spatial operator expressed in the frequency domain. The first uses a complex series of convolution sums to calculate $\hat{R}_k$ directly from $\hat{w}_k$. This approach is discarded due to its massive complexity (considering artificial dissipation schemes and turbulence modeling) and cost that scales quadratically with the number of modes $N$. Instead, we implement a pseudospectral approach in time. This approach requires several transformations between the physical and frequency domains that are performed by a fast Fourier transform (FFT). The computational cost of this transform scales like $N\log(N)$, where $N$ is a large number. A diagram detailing the transformations used by the pseudospectral approach is provided in Fig. 1.

The pseudospectral approach begins by assuming that $\hat{w}_k$ is known for all wave numbers. Using an inverse FFT, $\hat{w}_k$ can be transformed back to the physical space, resulting in a state vector $w(t)$ sampled at evenly distributed intervals over the time period. At each of these time instances, the steady-state operator $R[w(t)]$ can be computed. A FFT is then used to transform the spatial operator to the frequency domain in which $\hat{R}_k$ is known for all wave numbers. The unsteady residual $\hat{R^*}_k$ can then be calculated by adding $\hat{R}_k$ to the spectral representation of the temporal derivative $ikV\hat{w}_k$.

Consistent with the time-accurate approach, a pseudotime derivative can be added, and a time-stepping scheme can be employed to numerically integrate the resulting equations:

$$V\frac{\partial \hat{w}_k}{\partial \tau} + \hat{R^*}_k = 0 \tag{14}$$

In the NLFD case, an unsteady residual exists for each wave number used in the solution, and the pseudotime derivative acts as a gradient to drive the absolute value of all of these components to zero simultaneously.

The NLFD discrete adjoint equation can be developed using two separate approaches. In the first approach, we first take a variation of the unsteady residual $\hat{R^*}_k$, represented in Eq. (13) with respect to the state vector $\hat{w}_k$ and shape function $f$, to produce

$$\delta\hat{R^*}_k = ikV\delta\hat{w}_k + \delta\hat{R}_k$$

The next step would be to expand $\delta\hat{R}_k$ as a function of $\hat{w}_k$. As mentioned earlier, this approach would require a series of convolution sums to express $\delta\hat{R}_k$ as a function of $\delta\hat{w}_k$. This method

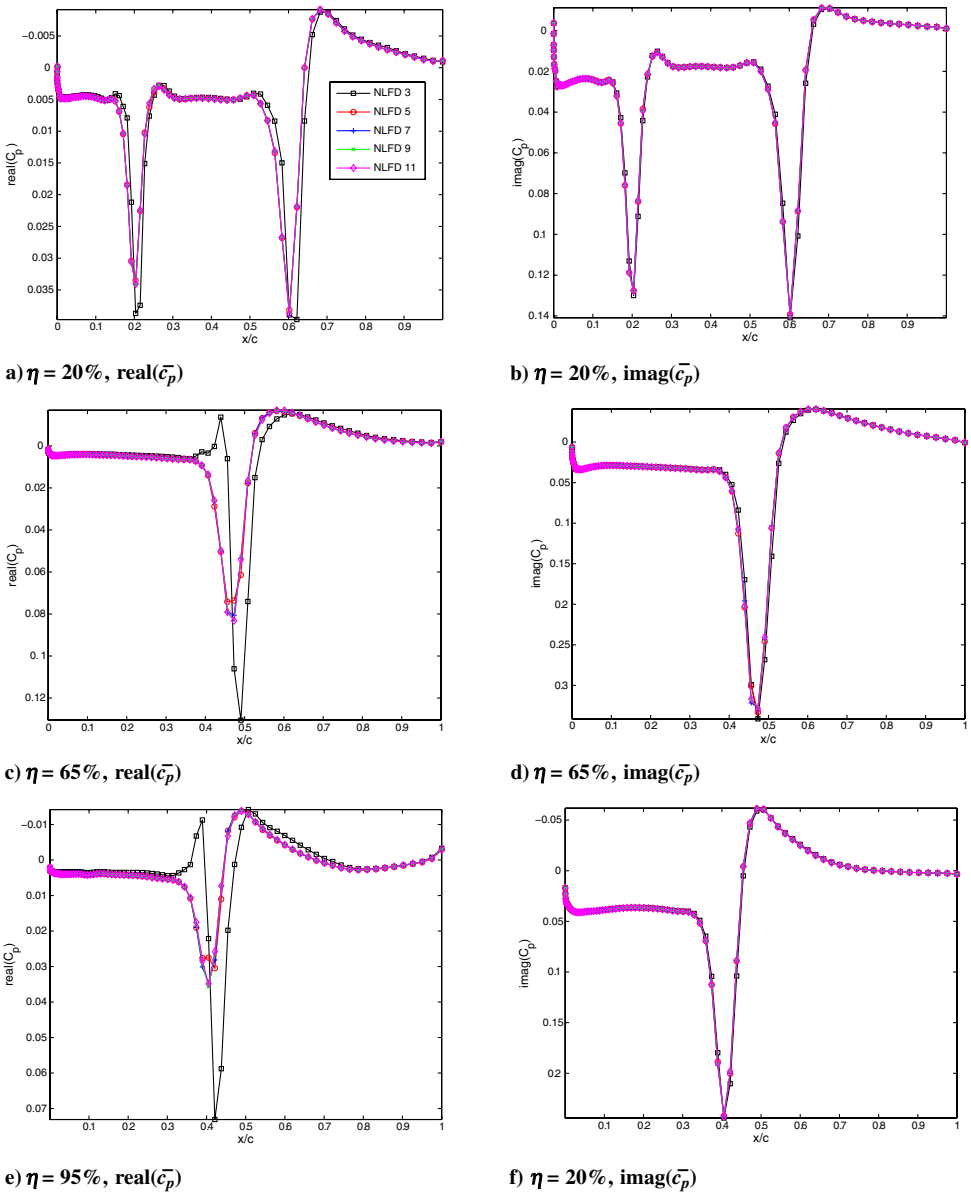


a) $\eta = 20\%$, real($\bar{c_p}$) b) $\eta = 20\%$, imag($\bar{c_p}$)

c) $\eta = 65\%$, real($\bar{c_p}$) d) $\eta = 65\%$, imag($\bar{c_p}$)

e) $\eta = 95\%$, real($\bar{c_p}$) f) $\eta = 20\%$, imag($\bar{c_p}$)

**Fig. 12 Comparison of the real and imaginary components of the first harmonic pressure coefficient for various modes and span stations.**

was not implemented due to its computational cost and added complexity. Instead, the adjoint equations were solved using a pseudospectral approach similar to the one applied to the flow equations.

In the latter approach, the NLFD adjoint equations are developed form the semidiscrete from of the adjoint equation, which can be as expressed as

$$V\frac{\partial \psi}{\partial t} + R(\psi) = 0$$

where $R(\psi)$ is the sum of all of the spatial operators, both convective and dissipative, used in the discretized adjoint equations. Refer to Nadarajah [7] for a detailed derivation of these spatial operators and boundary conditions. Next, we assume that the adjoint variable and spatial operator can be expressed as a Fourier series:

$$\psi = \sum_{k=-\frac{N}{2}}^{\frac{N}{2}-1} \hat{\psi}_k e^{ikt}, \qquad R(\psi) = \sum_{k=-\frac{N}{2}}^{\frac{N}{2}-1} \widehat{R(\psi)}_k e^{ikt} \tag{15}$$

The derivation of the NLFD adjoint then follows that of the NLFD flow equations. The NLFD adjoint equations are expressed as

$$V\frac{\partial \hat{\psi}_k}{\partial \tau} + \widehat{R(\psi)}_k^* = 0$$

where

$$\widehat{R(\psi)}_k^* = ikV\hat{\psi}_k + \widehat{R(\psi)}_k$$

The pseudospectral approach illustrated in Fig. 1 is employed in the NLFD adjoint code to form the unsteady residual. This term in conjunction with a pseudotime derivative provides an iterative solution process consistent with that documented for the flow equations.

## V. Optimization Procedure

In this paper, the inverse design boundary condition is applied to the near field, and sensitivity derivatives or the gradient are calculated on the airfoil surface. The gradient for the discrete adjoint is obtained by perturbing each point on the lower wall. Once the gradient $\mathcal{G}$ has been determined, it can be used to drive a variety of gradient-based search procedures. The search procedure used in this work is a descent method in which small steps are taken in the negative gradient direction. Let $\mathcal{F}$ represent the design variable and $\mathcal{G}$ the gradient. Then an improvement can be made with a shape change:

$$\delta\mathcal{F} = -\lambda\mathcal{G}$$

However, it is better to replace the gradient $\mathcal{G}$ by a smoothed value $\bar{\mathcal{G}}$ in the descent process. This acts as a preconditioner that allows the use of much larger steps and ensures that each new shape in the optimization sequence remains smooth. To apply smoothing in the $\xi_1$ direction, the smoothed gradient $\bar{\mathcal{G}}$ may be calculated from a discrete approximation to

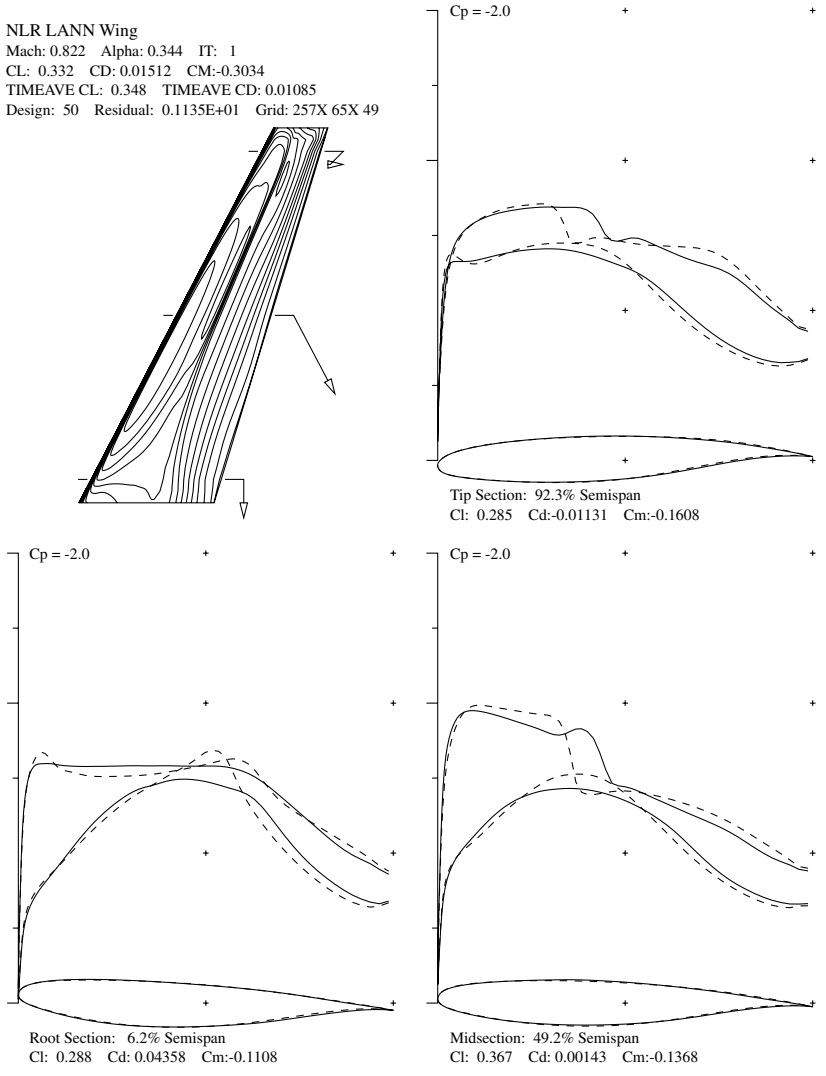


**Fig. 13 Initial and final pressure distribution for various span locations at a phase of 0-deg phase.**

$$\bar{\mathcal{G}} - \frac{\partial}{\partial \xi_1}\theta\frac{\partial \bar{\mathcal{G}}}{\partial \xi_1} = \mathcal{G}, \qquad \bar{\mathcal{G}} = 0$$

at the end points, where $\theta$ is the smoothing parameter. If the modification is applied on the surface, $\xi_2$ is constant, and then the first-order change in the cost function is

$$\delta I = -\iint \mathcal{G}\delta\mathcal{F}\,\mathrm{d}\xi_1 = -\lambda \iint \left(\overline{\mathcal{G}} - \frac{\partial}{\partial \xi_1}\theta\frac{\partial}{\partial \xi_1}\overline{\mathcal{G}}\right)\overline{\mathcal{G}}\,\mathrm{d}\xi_1$$
$$= -\lambda \iint \left[\overline{\mathcal{G}}^2 + \theta\left(\frac{\partial \overline{\mathcal{G}}}{\partial \xi_1}\right)^2\right]\mathrm{d}\xi_1 < 0$$

again guaranteeing an improvement unless $\bar{\mathcal{G}} = \mathcal{G} = 0$ and assuring an improvement if $\lambda$ is sufficiently small and positive.

In some problems, it turns out that the Hessian can be represented as a second-order differential operator, so that with a proper choice of the smoothing parameter, the method becomes the Newton method. Search methods were intensively evaluated in a recent study by Jameson and Vassberg [19], and it was verified that these sample problems (which may have a high linear content) could be solved with a number of search steps, independently of the number of design variables.

## VI. Design Process

The design process used in this work will change the shape of the wing to minimize its time-averaged coefficient of drag. Given the derivation provided in previous sections, the adjoint boundary condition can easily be modified to admit other figures of merit. The shape of the wing is constrained such that the maximum thickness-to-chord ratio remains constant between the initial and final designs. In addition, the mean angle of attack is allowed to vary to ensure the time-averaged coefficient of lift remains constant between designs.

The UFSYN107 developed by Nadarajah and Jameson [6], employs a nonlinear frequency-domain method in the solution of the unsteady Navier–Stokes equations. The NLFD adjoint-based design procedures require the following steps:

### A. Periodic Flow Calculation at Constant Time-Averaged Lift

A set of multigrid cycles is used to drive the unsteady residual to a negligible value for all of the modes used in the representation of the solution. In the case of a design process that constrains the time-averaged lift, the mean angle of attack is perturbed every 10 multigrid cycles to maintain a constant time-averaged coefficient of lift. This allows the unsteady residual to reduce by an order of two in magnitude before the angle is modified again.

### B. Adjoint Calculation

The adjoint equation is solved by integrating in reverse time. With minor modifications, the NLFD numerical scheme employed to

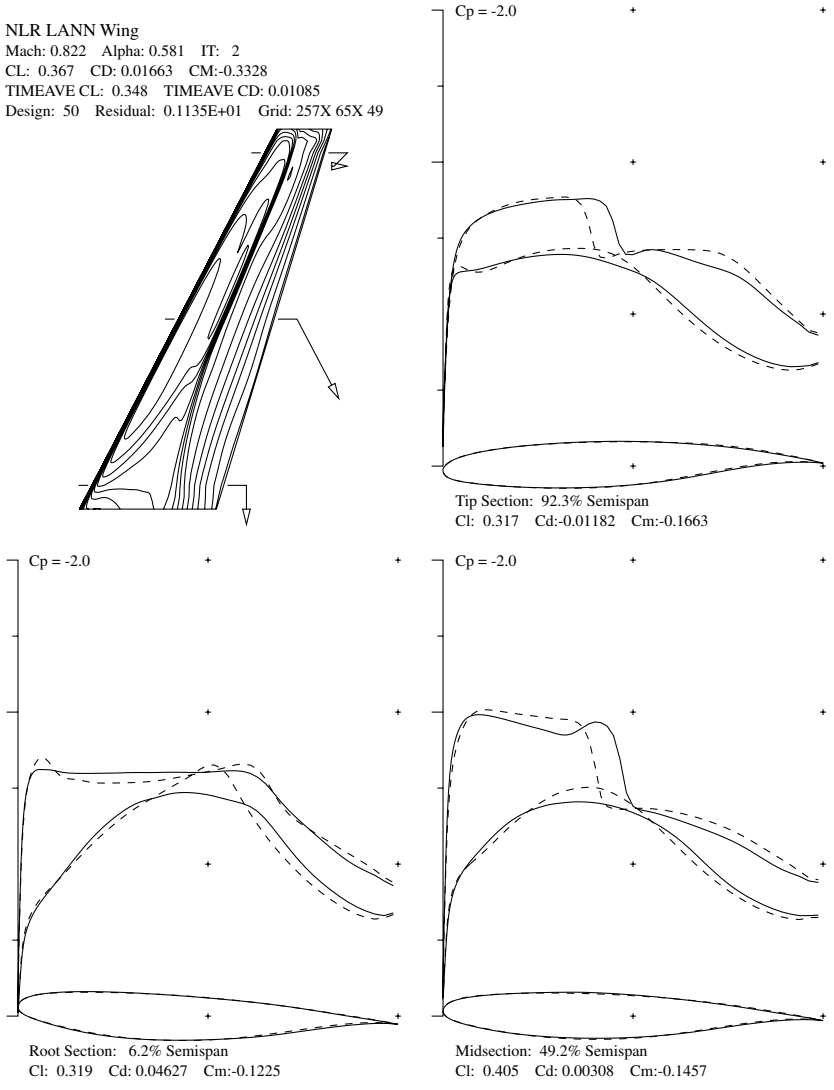


**Fig. 14 Initial and final pressure distribution for various span locations at a 72-deg phase.**

solve the flow equations is used to solve the adjoint equations in reverse time.

### C. Gradient Evaluation

An integral over the last period of the adjoint solution is used to form the gradient. This gradient is then smoothed using an implicit smoothing technique. This ensures that each new shape in the optimization sequence remains smooth and acts as a preconditioner that allows the use of much larger steps. The smoothing leads to a large reduction in the number of design iterations needed for convergence. Refer to Nadarajah and Jameson [6] for a more comprehensive overview of the gradient smoothing technique. An assessment of alternative search methods for a model problem is given by Jameson and Vassberg [19].

### D. Wing Shape Modification

The wing shape is then modified in the direction of improvement using a steepest-descent method. Let $\mathcal{F}$ represent the design variable and $\mathcal{G}$ the gradient. An improvement can then be made with a shape change:

$$\delta\mathcal{F} = -\lambda\mathcal{G}$$

### E. Grid Modification

The internal grid is modified based on perturbations on the surface of the wing. The method modifies the grid points along each grid index line projecting from the surface. The arc length between the surface point and the far-field point along the grid line is first computed, then the grid point at each location along the grid line is attenuated proportional to the ratio of its arc-length distance from the surface point and the total arc length between the surface and the far field.

### F. Repeat the Design Process

The entire design process is repeated until the objective function converges. The problems in this work typically required between 9 and 25 design cycles to reach the optimum.

## VII. Results

The following subsections present results from simulations of a three-dimensional wing undergoing a change in angle of attack as a function of time:

$$\alpha(t) = \alpha_o + \alpha_m \sin(\omega t)$$

For the cases presented in this section, the mean angle of attack $\alpha_o$ is 0.59 deg for the validation case and 0 deg for the design test cases. For both cases, the deflection angle $\alpha_m$ is set to $\pm 0.25$ deg. The reduced frequency, $\omega c/2V_\infty$, is set to 0.102, with a far-field Mach

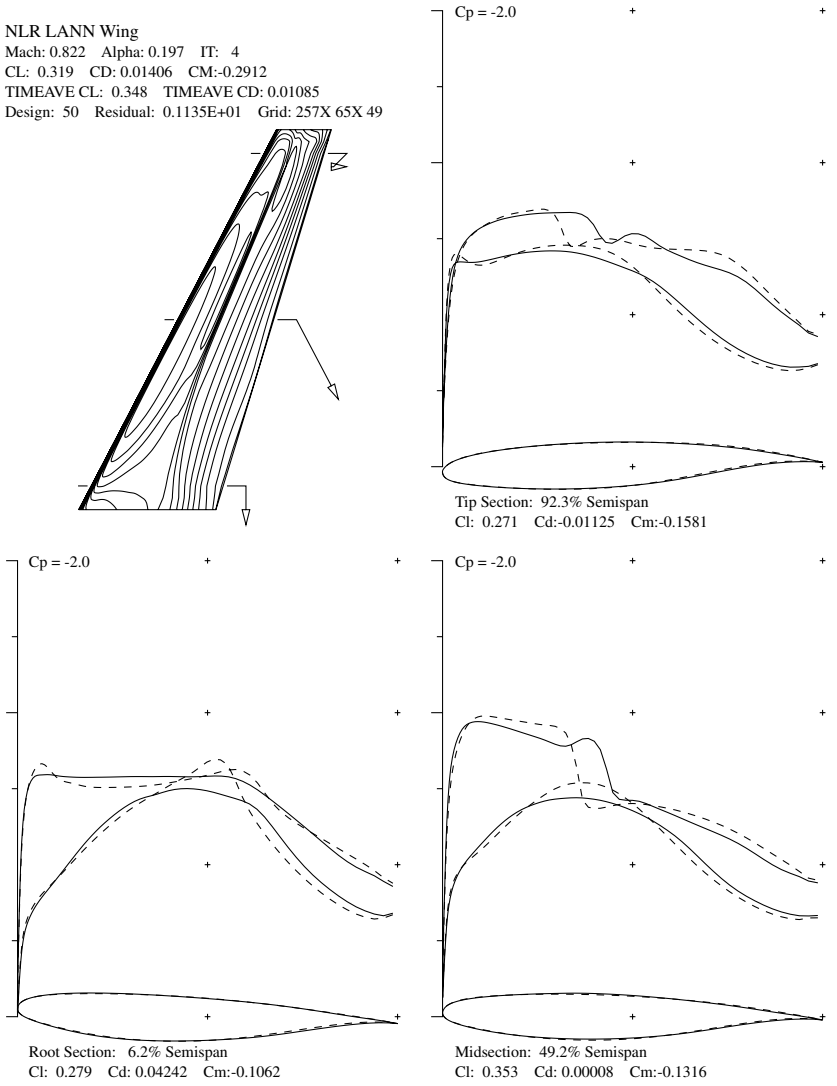


**Fig. 15 Initial and final pressure distribution for various span locations at a 216-deg phase.**

number $M_\infty$ of 0.822. The wing is pitched about the 61.2% of the root chord. The flight conditions are based on run 73 of the central transonic test case CT5, conducted by Zwaan [20] at the National Aerospace Laboratory/NLR.

The first part of the Results section contains a code-validation study. The study compares the convergence of the flow and adjoint solvers for various time steps per period and compares the lift hysteresis and drag and moment variation. This is necessary to quantify the required number of time steps per period to establish a periodic steady-state flow. The pressure distribution is compared with experimental data and prior inviscid results [15]. In the second subsection, a redesign of the LANN wing is demonstrated. Finally, a gradient comparison between various numbers of temporal modes and the convergence of the objective function is presented.

### A. Validation

The computational grid employed for the validation study is a structured grid, as illustrated in Fig. 2. The message-passing interface (MPI) [21] domain topology is based on $N_{p_i} = 4$, $N_{p_j} = 1$, and $N_{p_k} = 3$, where $N_p$ is the number of processors in each direction. Each processor contains a grid of size $n_x \times n_j \times n_k = 65 \times 65 \times 33$; the total grid is $257 \times 65 \times 97$. Cross-sectional views of the grid at the 20 and 65% span stations are shown in Fig. 3.

Figure 4 illustrates the convergence of the viscous NLFD flow solver. The convergence was obtained for the LANN wing test case for three, five, and seven time steps per period. The zeroth mode for all cases converge at the same rate; the same is true for the first, second, and third modes. The flow solver residual attains a reduction of four orders of magnitude over 2400 multigrid cycles. For the design cases, only 200 cycles were employed per design cycle. Figure 5 (use the Fig. 4 legend) illustrates the convergence of the viscous NLFD adjoint solver. Only 400 multigrid cycles were needed to converge the adjoint solver to the same level of accuracy as the flow solver. The rate of convergence is higher for the adjoint solver; all modes converge at similar rates.

The lift hysteresis is demonstrated in Fig. 6 for various numbers of time steps per period. Here, as indicated in the legend, NLFD 3 is synonymous to three time steps per period. As the wing oscillates at a small angle of attack, the shock wave moves back and forth about a mean location and is closely sinusoidal and lags the wing motion. This lag is evident in the lift hysteresis loop, in which the maximum lift does not occur at the maximum angle of attack. The nonlinear behavior of unsteady viscous transonic flows is primarily due to the movement of the shock, and this is evident in Fig. 6, which shows that one harmonic is sufficient to produce an accurate lift hysteresis. However, Fig. 7 demonstrates that at least two harmonics are needed to capture the variation of the drag coefficient versus angle of attack accurately. Figure 8 illustrates the variation in pitching moment and Fig. 9 demonstrates the variation of lift versus drag coefficient, further providing evidence that at least two harmonics are required to accurately capture the flowfield for the LANN wing, run 73.

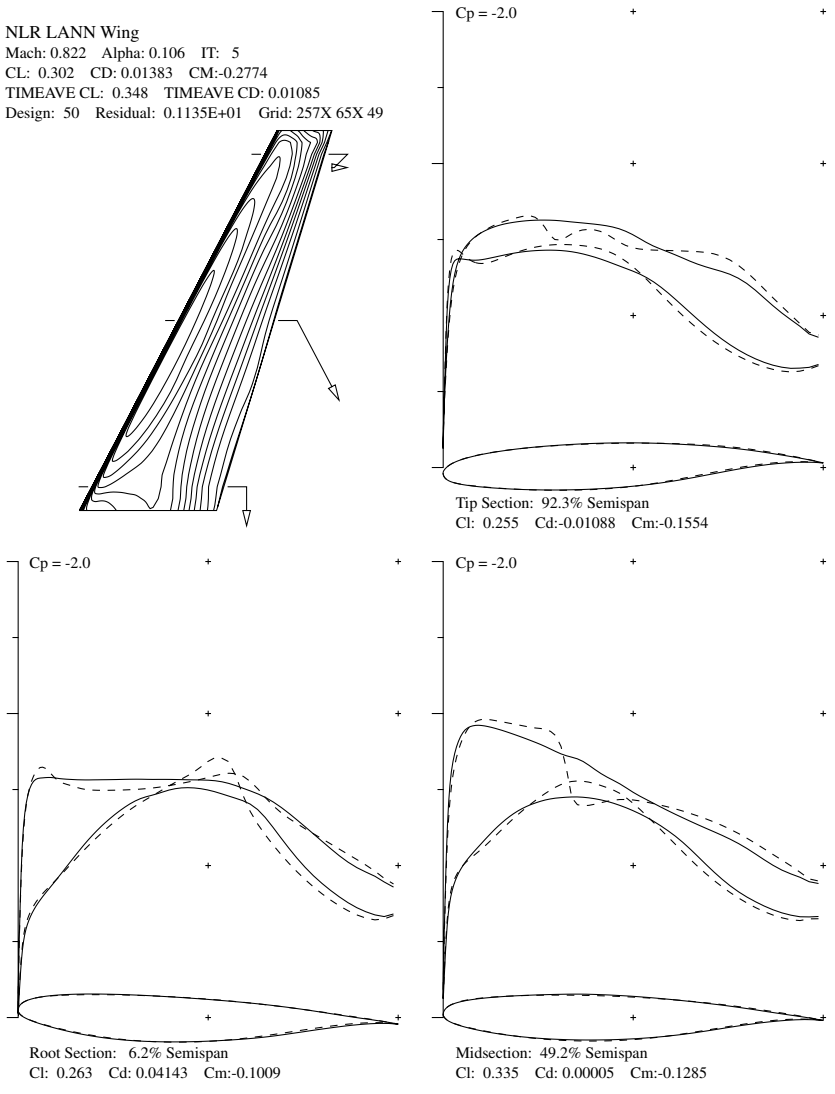


**Fig. 16 Initial and final pressure distribution for various span locations at a 288-deg phase.**

In Fig. 10, a validation of the surface pressure coefficient is presented. The figure illustrates the pressure distribution for two different angles of attacks at two separate span stations. In Fig. 10a, results based on both the inviscid and viscous NLFD methods are compared with experimental data at the span location $\eta = 20\%$ and angle of attack $\alpha = 0.59$ deg. The inviscid NLFD results compare closely to the viscous solutions, however, the location of the shock for the inviscid NLFD solution differs by 5% of the chord. This is an expected result, because the location of the shock is generally dependent on viscous effects, especially for unsteady flows. Apart from the shock location, the viscous NLFD solution resolves the peak pressure accurately. Nevertheless, both solutions differ from the experimental work, and further research is necessary to investigate the discrepancy. One possible reason for the difference could be due to the effect of the turbulence model on the unsteady viscous flows. This work has employed the Baldwin-Lomax model, which is an algebraic turbulence model. As part of future work, the authors are replacing the model with one based on the transport equations. The k-$\omega$ with and without the shear-stress transport (SST) correction and the Spalart–Allmaras models are being considered. Figures 10b–10d illustrate the comparison at the maximum angle of attack and at a different span location; similar trends are observed for these conditions. The difference in the shock location and strength at the $\eta = 65\%$ span station is larger.

A second important outcome of Fig. 10 is the required number of time steps per period or modes to accurately resolve the pressure distribution. At the 20% span station, the NLFD 3 viscous case is able to accurately produce the unsteady-flow solution. However, at the 65% span location, a slight discrepancy is observed at the shock location. Figures 10c and 10d contain insets that demonstrate the difference in the pressure distribution at the discontinuity among the three solutions. The $*$ solution corresponds to the three-time-step-per-period case; subsequently, the $\square$ corresponds to five and $\blacklozenge$ to seven time steps. The five- and seven-time-step cases compare very well. A greater departure of the pressure at the discontinuity produced by the three-time-step case is observed in Fig. 10d. This is a further indication that the viscous NLFD solutions require at least five time steps per period to resolve the flowfield, compared with the inviscid solution that only required three [15].

To further validate the NLFD approach for three-dimensional unsteady viscous flows, Fig. 11 demonstrates the pressure distribution for various NLFD solutions and experimental data at span stations 33, 47, 82.3, and 95%. At each span station, the figure shows the comparisons at the 0, 90, and 270-deg phases. The figure demonstrates that with just three time steps per period, the three-dimensional unsteady viscous flow over the entire wing is well represented. However, as seen from Fig. 10, five time steps will provide for a better pressure solution at the shock.

An investigation of the real and imaginary components of the first mode of the pressure coefficient is explored in Fig. 12. The figure describes the real and imaginary components at the 20, 65, and 95% span stations for various time steps per period. Two easily visible observations are as follows:

1) There is no distinctive difference in the imaginary component among the various cases for all three span stations.

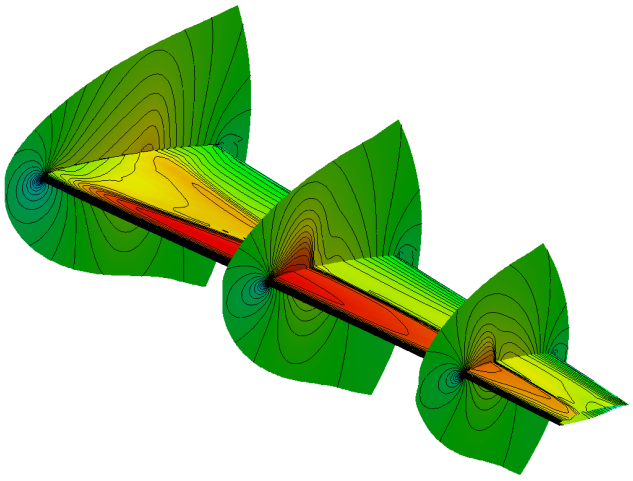

**a) Initial surface-pressure contour**

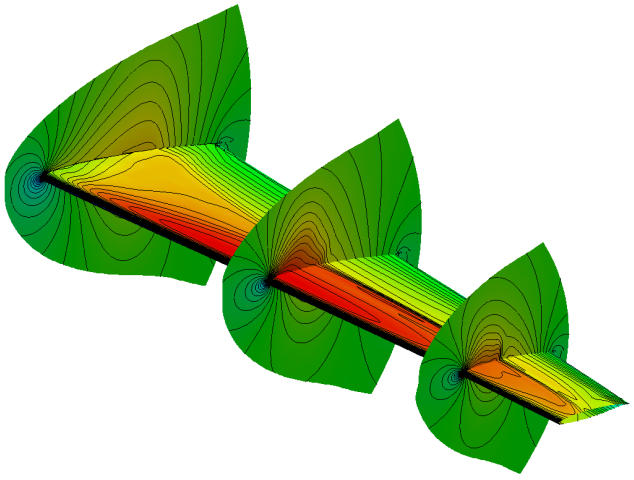

**b) Final surface-pressure contour**

**Fig. 17 Initial and final surface-pressure contours at a 0-deg phase for the LANN wing.**

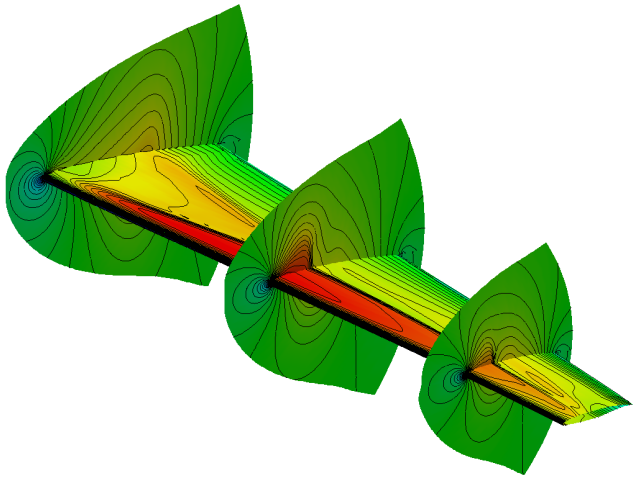

**a) Initial surface-pressure contour**

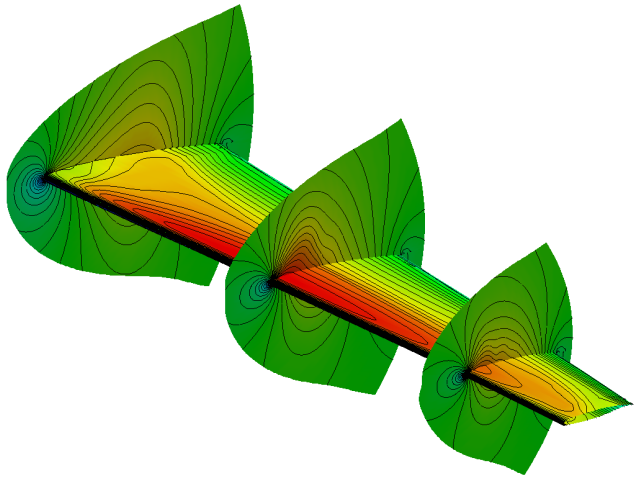

**b) Final surface-pressure contour**

**Fig. 18 Initial and final surface-pressure contours at a 288-deg phase for the LANN wing.**

2) The real component of the three-time-step case is vastly dissimilar from the higher temporal-resolution cases.

A closer observation of Figs. 12c and 12e reveals a third finding: there is a very minor difference over just three grid points between the five-time-step case and the 7-, 9-, and 11-time-step cases. The 9- and 11-time-step cases were computed in addition to the basic three cases shown thus far to provide a benchmark for the seven-time-step case. The figures illustrate that the seven-time-steps-per-period solution produced similar results to those for the 9 and 11 cases, however, the improvement is minimal and the five-time-step solution is adequate.

### B. LANN Wing Redesign

This section documents the results of the redesign of the LANN wing to reduce the time-averaged drag coefficient for a fixed time-averaged lift coefficient. The wing thickness ratio is constrained at each span station. The simulation was performed at a Mach number $M_\infty = 0.82$, reduced frequency $\omega_r = 0.102$, and deflection of $\pm 0.25$ deg about the 0-deg angle of attack. As established in the previous section, five time steps per period were needed to accurately represent the variation of the drag coefficient versus angle of attack and pressure distributions at various span stations and phases. Because the objective function is the time-averaged drag coefficient, five time steps will be used for the redesign of the LANN wing. This decision will be further supported with a gradient accuracy study at the end of this section.

During the initial stage to compute the flow solution, the time-averaged lift and drag are computed and used as the target lift and objective function. During the subsequent design cycles, the mean angle of attack is modified at every ten multigrid cycles to maintain the time-averaged lift coefficient. Ten multigrid cycles were chosen to allow the flowfield to develop and to reduce the initial peak transient solutions admitted into the solution due to the change in angle of attack. At each design cycle, 200 multigrid cycles were used.

Figures 13–16 illustrate the wing-surface-pressure contour and the initial and final pressure distributions at three span locations at the 0, 72, 216, and 288-deg phases after 50 design cycles. In Fig. 13, the pressure contour illustrates the severe weakening of the λ-shock system, and this is further validated in the three pressure-coefficient plots at span stations 6.2, 49.2, and 92.3%. The initial pressure distribution is illustrated as a dotted line, and the solid line is at the final design. The plots show a reduction of the shock-wave strength at the midsection, with a decrease in the sectional drag coefficient from 0.0027 to 0.0014. The mean angle of attack was perturbed from the initial 0 to 0.344 deg to maintain the time-averaged lift coefficient at 0.348. The time-averaged drag coefficient reduced by 5.65% from 0.0115 to 0.01085 within 50 design cycles. The design is halted once the change in the objective function or time-averaged drag coefficient reaches a level of 1.E-6. The figure also demonstrates the initial and final, illustrated by a dotted line and a solid line, cross-sectional airfoil profiles. A distinctive feature of the new airfoil is the reduction of the upper-surface curvature. The reduced curvature contributes to the weakening of the shock wave in the midsection region of the LANN wing. At the 72, 216, and 288-deg phases, as illustrated in Figs. 14–16, a severe weakening of the shock wave in the mid and tip sections of the LANN wing are observed. At the 288-deg phase, a complete elimination of the shock wave is demonstrated.

Figures 17 and 18 demonstrate the initial and final three-dimensional surface-pressure contours at the 0 and 288-deg phases.

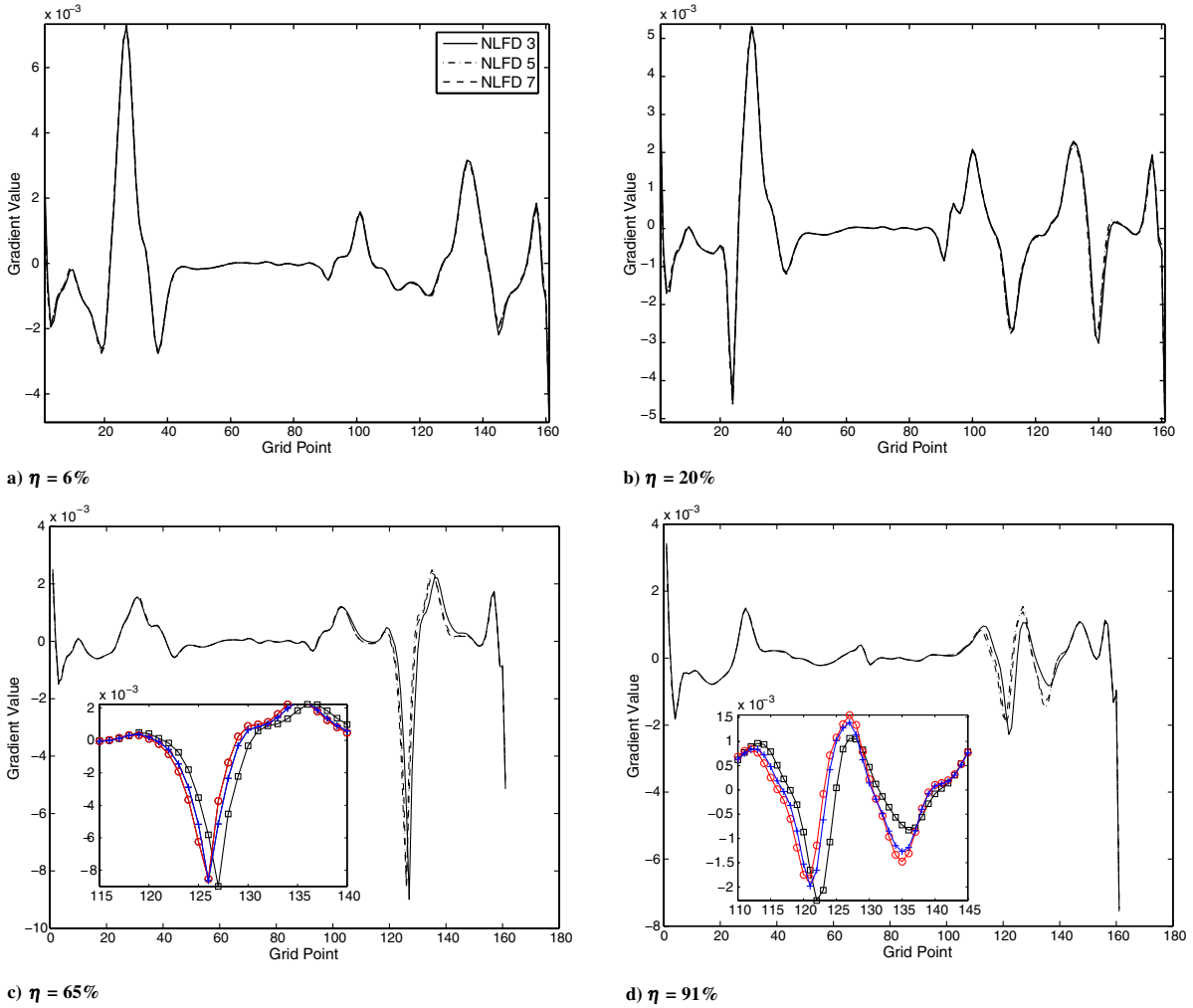


**Fig. 19 Comparison of gradients for various modes for the LANN wing.**

The weakening of the λ shock is demonstrated in Fig. 17b. A complete elimination of the shock is observed at the 288-deg phase.

The Validation subsection illustrated the ability of the NLFD method to accurately model the flow with only five time steps per period. However, for the case of optimum shape design, the accuracy of the gradient of the objective function is of paramount importance. Figure 19 illustrates the gradients of the objective function at four different span locations for various temporal resolutions. The gradients are plotted in a clockwise direction, starting from the lower trailing edge to the leading edge and ending at the upper trailing-edge point. The figures illustrate that with just three time steps per period, the gradients can be accurately captured at the 6 and 20% span stations; however, an additional mode or five time steps per period are required at the 65 and 91% stations. The gradients over a vast majority of the points at these stations agree very well; however, a large difference is observed between the 120 and 140 grid points. The points are adjacent to the shock location and, as seen in the pressure-distribution comparisons in Figs. 10c and 10d, an additional mode is required to resolve the gradient. The insets further illustrate the difference between the gradient values. Here, the ∗ solution corresponds to the three-time-step-per-period case; subsequently, □ corresponds to five and ◆ to seven time steps.

Finally, Fig. 20 presents the convergence of the time-averaged drag coefficient from 115 drag counts to 108.5. The similarity between the initial and final span loading, as shown in Fig. 21, indicates that the lift-induced drag coefficient has remained constant. Therefore, the decrease in the time-averaged drag is mainly due to the reduction in the wave drag. Figure 22 shows the convergence of $\Delta I$, where $I$ is the objective function (time-averaged drag coefficient) and $\Delta I$ reaches a level of 1.E-6 within 50 design cycles. During the first 35 design cycles, $\Delta I$ converges linearly, as expected. Linear convergence is characteristic of a steepest-descent type of method. As the final wing profile is realized, the convergence increases rapidly. The code is automatically stopped as soon as a change of 1E-6 is detected. This level of change corresponds to a change to the sixth decimal place of the drag coefficient, and this is sufficient for engineering accuracy.

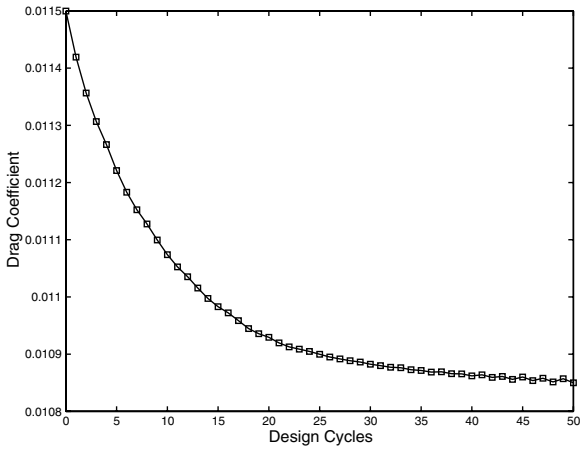


**Fig. 20 Convergence of the time-averaged drag coefficient.**

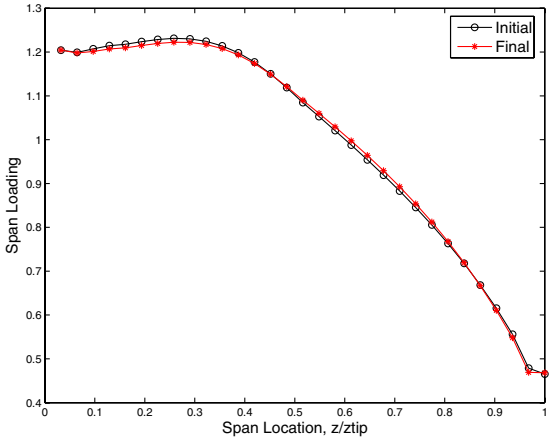


**Fig. 21 Initial and final span loading.**

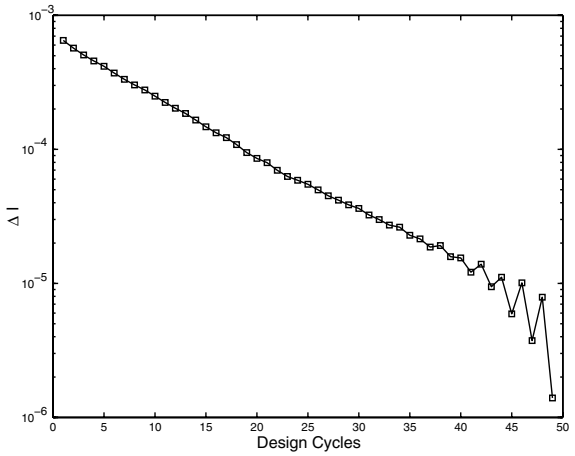


**Fig. 22 Convergence of the change in the objective function $\Delta I$.**

## VIII. Conclusions

The NLFD method requires just five time steps per period to resolve the unsteady viscous transonic flowfield. A redesign of the LANN wing was demonstrated, with a reduction of the time-averaged drag coefficient by 5.65% while maintaining the time-averaged lift coefficient constant. The NLFD method with five time steps per period also provides accurate gradients. These results further demonstrate the potential of the method to provide significant improvements to more realistic problems such as helicopter rotors, turbomachinery, and other unsteady devices operating in the transonic regime.

## References

[1] Jameson, A., "Computational Aerodynamics for Aircraft Design," *Science*, Vol. 245, 1989, pp. 361–371.

[2] Jameson, A., "Optimum Aerodynamic Design Using CFD and Control Theory," AIAA 12th Computational Fluid Dynamics Conference, San Diego, CA, AIAA Paper 95-1729, June 1995.

[3] Nadarajah, S., Jameson, A., and Alonso, J. J., "Sonic Boom Reduction Using an Adjoint Method for Wing-Body Configurations in Supersonic Flow," 9th AIAA/ISSMO Symposium on Multidisciplinary Analysis and Optimization Conference, Atlanta, GA, AIAA Paper 2002-5547, Sept. 2002.

[4] Reuther, J., Alonso, J. J., Rimlinger, M. J., and Jameson, A., "Aerodynamic Shape Optimization of Supersonic Aircraft Configurations via an Adjoint Formulation on Parallel Computers," 6th AIAA/NASA/ISSMO Symposium on Multidisciplinary Analysis and Optimization, Bellevue, WA, AIAA Paper 96-4045, Sept. 1996.

[5] Reuther, J., Jameson, A., Farmer, J., Martinelli, L., and Saunders, D., "Aerodynamic Shape Optimization of Complex Aircraft Configurations via an Adjoint Formulation," 34th Aerospace Sciences Meeting and Exhibit, Reno, NV, AIAA Paper 96-0094, Jan. 1996.

[6] Nadarajah, S., and Jameson, A., "Optimal Control of Unsteady Flows Using a Time Accurate Method," 9th AIAA/ISSMO Symposium on Multidisciplinary Analysis and Optimization Conference, Atlanta, GA, AIAA Paper 2002-5436, Sept. 2002.

[7] Nadarajah, S., "The Discrete Adjoint Approach to Aerodynamic Shape Optimization," Ph.D. Dissertation, Department of Aeronautics and Astronautics, Stanford Univ., Stanford, CA, Jan. 2003.

[8] Jameson, A., "Time Dependent Calculations Using Multigrid, with Applications to Unsteady Flows Past Airfoils and Wings," AIAA 10th Computational Fluid Dynamics Conference, Honolulu, HI, AIAA Paper 91-1596, June 1991.

[9] Adamczyk, J. J., "Model Equation for Simulating Flows in Multistage Turbomachinery," NASA TM-86869, Nov. 1984.

[10] Hall, K. C., Thomas, J. P., and Clark, W. S., "Computation of Unsteady Nonlinear Flows in Cascades Using a Harmonic Balance Technique," *AIAA Journal*, Vol. 40, No. 5, May 2002, pp. 879–886; also AIAA Paper 0001-1452.

[11] McMullen, M., Jameson, A., and Alonso, J., "Acceleration of Convergence to a Periodic Steady State in Turbomachinery Flows," 39th Aerospace Sciences Meeting and Exhibit, Reno, NV, AIAA Paper 2001-0152, Jan. 2001.

[12] McMullen, M., Jameson, A., and Alonso, J., "Application of a Non-Linear Frequency Domain Solver to the Euler and Navier–Stokes Equations," 40th Aerospace Sciences Meeting and Exhibit, Reno, NV, AIAA Paper 2002-0120, Jan. 2002.

[13] McMullen, M., "The Application of Non-Linear Frequency Domain Methods to the Euler and Navier–Stokes Equations," Ph.D. Dissertation, Department of Aeronautics and Astronautics, Stanford Univ., Stanford, CA, Mar. 2003.

[14] Nadarajah, S., McMullen, M., and Jameson, A., "Optimum Shape Design for Unsteady Flows Using Time Accurate and Non-Linear Frequency Domain Methods," 16th Computational Fluid Dynamics Conference, Orlando, FL, AIAA Paper 2003-3875, June 2003.

[15] Nadarajah, S., McMullen, M., and Jameson, A., "Non-Linear Frequency Domain Method Based Optimum Shape Design for Unsteady Three-Dimensional Flows," AIAA 44th Aerospace Sciences Meeting and Exhibit, Reno, NV, AIAA Paper 2006-1052, Jan. 2006.

[16] Duta, M. C., Giles, M. B., and Campobasso, M. S., "The Harmonic Adjoint Approach to Unsteady Turbomachinery Design," *International Journal for Numerical Methods in Fluids*, Vol. , Oct. 200240, pp. 323–332.

[17] Thomas, J. P., Hall, K. C., and Dowell, E. H., "A Discrete Adjoint Approach for Modelling Unsteady Aerodynamic Design Sensitivities," 41th Aerospace Sciences Meeting and Exhibit, Reno, NV, AIAA Paper 2003-0041, Jan. 2003.

[18] Jameson, A., Schmidt, W., and Turkel, E., "Numerical Solutions of the Euler Equations by Finite Volume Methods with Runge-Kutta Time Stepping Schemes," AIAA Paper 81-1259, Jan. 1981.

[19] Jameson, A., and Vassberg, J. C., "Studies of Alternative Numerical Optimization Methods Applied to the Brachistochrone Problem," *Computational Fluid Dynamics*, Vol. 9, No. 3, 2000, pp. 281–296.

[20] Zwaan, R. J., "*Data Set 9, LANN Wing. Pitching Oscillation*, AGARD, Rept. R-702, Addendum No. 1, 1985.

[21] *Message Passing Interface Forum* [online database], http://www.mpi-forum.org/ [retrieved Feb. 2003].